Chemical Engineering Journal 464 (2023) 142725

Contents lists available at ScienceDirect

Chemical Engineering Journal

journal homepage: www.elsevier.com/locate/cej

Multi-scale nanofiber membrane functionalized with metal-organic frameworks for efficient filtration of both $PM_{2.5}$ and CH_3CHO with colorimetric NH_3 detection

Ji Hyun Lee [a,b], Hyun Ju Oh [a], Young Ki Park [a], Yoonjin Kim [a], Gyudong Lee [a], Song Jun Doh [a], Woosung Lee [a], Seon-Jin Choi [b,*], Ki Ro Yoon [a,c,*]

[a] Advanced Textile R&D Department, Korea Institute of Industrial Technology, 143, Hanggaulro, Sangnok-gu, Ansan-si, Gyeonggi-do 15588, Republic of Korea
[b] Division of Materials Science and Engineering, Hanyang University, 222, Wangsimni-ro, Seongdong-gu, Seoul 04763, Republic of Korea
[c] HYU-KITECH Joint Department, Hanyang University, 222, Wangsimni-ro, Seongdong-gu, Seoul 04763, Republic of Korea

ARTICLE INFO

Keywords:
Electrospinning
Nanofiber/nanonet membrane
Metal–organic frameworks
Air filtration media
Colorimetric sensor
Toxic gas adsorption

ABSTRACT

Air filtration technology for mitigating pollution due to harmful mixtures of particulate matter (PMs) and yellow dust has been continuously improved. However, significantly small-sized airborne contaminants, such as $PM_{2.5}$, and toxic gases, including volatile organic compounds (VOCs), remain in the atmosphere and critically affect the human health. Therefore, the development of an integrated filtration system with fast detection and high removal efficiency toward various airborne pollutants without significant interference from airflow is required. Herein, we designed a hybrid air filtration system comprising a colorimetric multi-scale nanofiber (NF)/nanonet (NN) membrane and a metal–organic framework (MOF)-decorated mesh substrate to remove $PM_{2.5}$ and toxic gases in the air. The electrospinning of a halochromic dye (bromocresol purple; BCP) with a polyacrylonitrile solution spontaneously forms spider-web-like NN networks between NFs, which significantly improves the filtration efficiency, particularly for sub-120 nm aerosol particles with a high quality factor of 0.0387 Pa^{-1}. The BCP components in the NF/NN membrane demonstrated ultrafast and reversible colorimetric sensing properties within 5 s when exposed to 20 ppm ammonia gas. Furthermore, the adsorptive UiO-66-NH_2 MOF-grown macroporous mesh contributes to the removal of acetaldehyde as well as provides an efficient membrane support with negligible increase in the pressure drop.

1. Introduction

Owing to the accelerated industrial development, global air pollution has emerged as a critical issue, adversely affecting public and human health.[1,2] Air pollution mainly arises from burning fossil fuels (e.g., coal, oil, and gasoline) for electrical power generation, home heating, and vehicle transport, resulting in significantly increased emissions of global warming gases, such as ozone, nitrogen oxides (NO_x), sulfur dioxide and carbon mono/dioxides.[3–6] Furthermore, primary and secondary particulate matters (PMs), derived from industrial emissions, have been considered significant factors.[7,8] As majority of people spend approximately 87% of their time indoors,[9] the issue of air pollution has been extended to indoor environments.[10,11] Indoor-generated volatile organic compounds (VOCs) originating from furniture polish, smoke, pesticides, and electronic products adversely affect human health, even in very small amounts.[12,13] Therefore, it is necessary to develop advanced filtration technologies, which can simultaneously remove PMs and toxic VOCs, for effective indoor air quality control.

Recently, nonwoven fibrous filters with diameters less than a few dozen micrometers have been developed as filtration membranes for PM removal. As a fibrous platform, melt-blown (MB) fibrous filters have been widely adopted for manufacturing face masks and household and industrial filters because they are composed of several micron-scale fibers and can be produced in a high yield.[14,15] MB filters store abundant charges during the production process and generate a quasi-permanent electric field around the microfibers via electret attraction, which significantly improves the filtration efficiency toward PMs.

* Corresponding authors at: Advanced Textile R&D Department, Korea Institute of Industrial Technology, 143, Hanggaulro, Sangnok-gu, Ansan-si, Gyeonggi-do 15588, Republic of Korea (K.R. Yoon).
E-mail addresses: sjchoi27@hanyang.ac.kr (S.-J. Choi), kryoon@kitech.re.kr (K.R. Yoon).

https://doi.org/10.1016/j.cej.2023.142725
Received 8 December 2022; Received in revised form 27 February 2023; Accepted 31 March 2023
Available online 1 April 2023

However, because this mechanism relies heavily on electrostatic deposition, the static electricity formed on the fiber surface is dissipated by the environmental humidity over time; thereby significantly reducing the filtration efficiency.[16] In contrast, electrospinning is a versatile method suitable for the large-scale fabrication of nanometer-scale nonwoven fibers with relatively constant diameters. Electrospun nanofibers (NFs) can filter via non-electrostatic attractions; therefore, they are not susceptible to humidity. The electrospun NFs contain extremely small and uniform pores originating from the sub-micron-level fiber diameters, which can yield high filtration efficiency although they have a thin filter medium.

Porous adsorbent materials are beneficial for capturing gaseous pollutants.[17–19] In particular, metal–organic frameworks (MOFs) offer very large specific surface areas and highly tunable adsorptive properties through a diverse structural combination of various central metal ions and organic ligands. To simultaneously filter PMs and gaseous pollutants, a hybrid membrane combining an adsorptive MOF and non-electrostatic filtration media has been previously demonstrated.[11,20,21] For instance, Wang et al. reported a strategy to fabricate an air filter by manufacturing electrospun NFs with dispersed MOF powders (ZIF-8, Mg-MOF-74, UiO-66-NH_2, and MOF-199) to effectively remove $PM_{2.5}$ and SO_2.[22] However, the presence of MOF particles between NF layers leads to a significant reduction in the pore size of the filter, causing a large pressure drop and a decrease in airflow.[21] Therefore, a tailored design of filtration media that comprise both MOF particles and NFs is important to gain the unique advantages of the two components without mutual interference, which determines the quality of air filtration.

Herein, we propose an ideal configuration of MOF and electrospun NF hybrids for filtering both $PM_{2.5}$ and toxic gases with significantly improved performance. We used an adsorptive Zr-based MOF (UiO-66-NH_2) grown on a poly(ethylene terephthalate) (PET) mesh (MOF@mesh) as a macroporous substrate to support the electrospun NF membrane. We added bromocresol purple (BCP) into a solution of polyacrylonitrile (PAN) in N,N-dimethylformamide (DMF). The resulting mixture was subsequently electrospun, resulting in a unique spider-web-like NF/nanonet (NN) hybrid structure. The unique hierarchical fibrous structure exhibited a high filtration efficiency and quality factor (Q_f) of 86.2% and 0.0387 Pa^{-1}, respectively, owing to the enhancement of the physical sieving of sub-100 nm particles by locally distributed NN regions. The NF/NN membrane also exhibited an outstanding colorimetric response to BCP components when exposed to 20 ppm ammonia (NH_3). Furthermore, a hybrid NF/NN integrated with the MOF@mesh filter showed excellent adsorptive properties toward acetaldehyde (CH_3CHO) while maintaining high air permeability (17.8 $cm^3\ cm^{-2}\ s^{-1}$). We demonstrated the feasibility of using the developed filter as a window-type air filtration platform for effective indoor air quality control. We expect that a novel strategy for combining adsorptive MOFs and electrospun NFs can be widely used for various industrial air filtration applications that require the simultaneous control of various PMs and toxic gases.

2. Experimental section

2.1. Oxygen plasma treatment of macro-porous PET mesh

To improve the adhesion of the microporous PET mesh surface, the mesh was plasma-treated in a plasma chamber. The plasma treatment conditions were as follows: oxygen atmosphere, oxygen flow rate of 160 sccm, operating power of 200 W, generation time of 10 min, and generation frequency of 50 kHz.

2.2. Preparation of MOF powder

The UiO-66-NH_2 powder for evaluation was fabricated using the following synthetic method: 0.2 g of $ZrCl_4$ (≥ 99.9%, Sigma-Aldrich) was dissolved in 37.5 mL of DMF (≥99.8%, Sigma-Aldrich, 37.5 mL) and vigorously stirred to obtain a transparent solution. Thereafter, 1.425 mL of acetic acid (≥ 99%, Sigma-Aldrich) as a modulating agent was added to the transparent solution and stirred. Next, 0.155 g of 2-aminoterephthalic acid (NH_2-H_2BDC, 99%, Sigma-Aldrich) powder was dissolved in 12.5 mL of DMF (12.5 mL) to prepare an organic linker solution. The $ZrCl_4$ solution and NH_2-H_2BDC solution were poured into an autoclave, which was placed in oven at 130 °C overnight. After cooling, the mixture was centrifuged, washed, and fully dried at 60 °C to obtain the UiO-66-NH_2 crystals.

2.3. Preparation of MOF@mesh

First, 0.6 g $ZrCl_4$ was loaded into a glass vial and dissolved in 112.5 mL of DMF via 10 min of sonication. Thereafter, 4.275 mL of acetic acid was added to the solution, followed by stirring for 1 h. Next, 0.465 g NH_2-H_2BDC was loaded into a glass vial and dissolved in DMF (37.5 mL) to produce the organic linker solution. The $ZrCl_4$ solution, NH_2-H_2BDC solution, oxygen-treated mesh, and 187.5 μL of deionized (DI) water were poured into an Erlenmeyer glass flask, which was placed on a hot plate at 130 °C and stirred for 24 h. After cooling to room temperature, the stirred mesh was purified by washing it with DMF and ethanol. Finally, it was dried overnight in a vacuum oven at a reduced pressure and 60 °C.

2.4. Fabrication of the NF/NN on MOF@mesh filter

A BCP (Alfa Aesar)-added PAN (MW = 150,000 g mol^{-1}, Sigma-Aldrich)-based NF/NN membrane was prepared on the MOF@mesh using electrospinning. First, the PAN solution was prepared by adding 1 g PAN to 10 g DMF. To prepare samples with various BCP concentrations (0.0, 0.5, 1.0, 1.5, and 2.0 wt%), an appropriate amount of BCP powder was dissolved in the PAN solution under continuous vigorous stirring at 70 °C for 12 h. The stirred solution was transferred into a 12 mL syringe, and a 25 gauge needle was capped on the syringe tip. A feeding rate of 0.9 mL h^{-1} and high voltage of 12.9 kV were applied between the needle and drum collector wrapped in the MOF@mesh, which were separated by a distance of 15 cm.

2.5. Material characterizations

The microstructures of the fabricated filters were observed using field-emission SEM (FE-SEM; SU8010, Hitachi Co., Tokyo, Japan), and the surface bonding configurations were investigated via FT-IR spectroscopy (Spectrum Two, PerkinElmer Inc., MA, USA). The crystalline structure of the MOF particles was analyzed via XRD. The porous structure and BET surface area of the MOF crystals were evaluated using a surface area analyzer (ASAP 2010, Micromeritics, GA, USA). A capillary flow porometer (CFP-1500AEX, Porous Materials Inc., NY, USA) was used to estimate the pore diameter of the NF and NF/NN membranes. TGA (Q500, TA Instruments, DE, USA) was performed to estimate the thermal stability of membranes at a heating rate 20 °C min^{-1} in a nitrogen atmosphere in the temperature range of 40–800 °C. The visible light transmittance of the samples was measured using an ultraviolet–visible spectrophotometer and was calculated using the following equation:

$$\boldsymbol{Transmittance}(\%) = \boldsymbol{T}/\boldsymbol{T}_0 \quad (1)$$

where T_0 is transmittance of BCP_0.0, and T is the transmittance of BCP_0.5, BCP_1.0, BCP_1.5, or BCP_2.0.

2.6. Filtration performance tests

Air permeability data were collected using an air permeability tester (FX 3300) at a test pressure of 125 Pa. The samples were clamped over

the air inlet using test heads, after which the air was sucked through the pump. The preset test pressure was automatically maintained, and the air permeability of the filters was calculated in $cm^3\ cm^{-2}\ s^{-1}$. The particulate respiration filter performances of filtration efficiency, and pressure drop were measured using an automated air filtration tester (TSI 8130; TSI Inc., MN, USA). The flow rate was set to 32 L min^{-1} with sodium chloride (NaCl) aerosol particles of 50–260 nm diameters. When the NaCl particle passed through filter media, the upstream and downstream aerosol concentrations were measured simultaneously using a photometer system consisting of a laser and optics. The filtration efficiency (η) was calculated using the equation $\eta = (C_{up} - C_{down})/C_{up}$, where C_{up} and C_{down} are the NaCl concentrations upstream and downstream, respectively.

2.7. NH_3 gas-sensing test of the colorimetric NF/NN on MOF@mesh

The gas-sensing test system was designed to measure the color change of each filter in real time while being exposed to NH_3 gas. After exposure to NH_3 gas, the active color change of the sample was estimated using a color-eye 7000A spectrophotometer (X-rite, Grand Rapids, MI, USA). The color differences (ΔE) and surface color strength (K/S) were calculated using the following equations:

$$\Delta E = \sqrt{(\Delta L^*)^2 + (\Delta a^*)^2 + (\Delta b^*)^2} \quad (2)$$

where L* is the lightness; a* represents the red/green component, and b* represents the yellow/blue component·NH_3 gas was used at a concentration of 20 ppm, and the ΔE was measured for 300 s at 5 s-intervals.

2.8. Gas adsorption test

Gas adsorption characteristics were investigated using CH_3CHO, a VOC. Each sample was placed in a 2 L Tedlar® gas bag that was sealed, evacuated, and injected with 100 ppm CH_3CHO/N_2 gas. The concentration of injected CH_3CHO decreased over time due to adsorption onto the samples, which was measured at 10 min intervals for 60 min and at 120 min using a gas detector with detection tubes. The decrease in the amount of CH_3CHO gas was measured every 10 min for 2 h.

3. Results and discussion

The fabrication procedure for the hybrid NF/NN on MOF@mesh filter is schematically illustrated in Fig. 1. First, we directly synthesized UiO-66-NH_2 as an adsorptive MOF on a porous substrate, that is, a PET mesh with an air permeability of 645.4 $cm^3\ cm^{-2}\ s^{-1}$ (Fig. S1 and S2). To improve the affinity between the MOF and surface of PET mesh, O_2 plasma treatment was performed on the PET mesh for 10 min.[23] The O_2 plasma-treated PET mesh was then immersed in a precursor solution containing $ZrCl_4$ and NH_2-H_2BDC, and thereafter, solvothermal reaction was conducted at 130 °C under stirring for 24 h. After washing and subsequent drying, octahedral UiO-66-NH_2 MOF particles were uniformly grown on the surface of the PET mesh to obtain MOF@mesh, without a severe aggregation or blocking of pores. Next, the electrospinning of the PAN-based solution containing BCP at various concentrations (0.0–2.0 wt%) was performed on the MOF@mesh substrate. During electrospinning, a spider web-like NN structure was partially formed, covering the porous MOF@mesh substrate. Microstructural and chemical characterizations were performed using hybrid NF/NN on MOF@mesh filters and their filtration performance toward both PMs and VOCs was demonstrated.

The presence of BCP in the NF/NN membranes was confirmed by thermogravimetric analysis (TGA). The addition of BCP gradually increases the remaining weight of the membranes after the decomposition of NF/NN (Fig. S3). This result implies that residual BCP molecules inside the polymeric chains affect their thermal stability. SEM images of NF/NN membranes with various BCP contents are shown in Fig. 2a–i. The pristine PAN NFs (BCP_0.0) (Fig. 2a) exhibit a randomly entangled fiber network with uniform fiber diameters in the range of 250–290 nm. In contrast, the addition of BCP (BCP_0.5, 1.0, 1.5, and 2.0) induces the partial formation of spider-web-like NNs between the entangled NFs (Fig. 2b–2i). These NNs have a small diameter in the range of 30–60 nm and are locally distributed over the entire NF network. As the BCP concentration increases from 0.5 to 2.0 wt%, the density of NNs increases, whereas the overall pore sizes decrease. These distinctive morphologies are attributed to the BCP-induced phase separation of charged droplets during electrospinning caused by the instability of ejected fibers,[24–27] which results in the microstructural evolution of electrospun NFs with partially formed NNs between NFs.[28,29] The presence of such NF/NNs structures is advantageous for particulate filtration via physical sieving of small particles, such as fine dust or $PM_{2.5}$.

The surface chemical compositions of the membranes were investigated using FT-IR spectroscopy (Fig. 2j). For all samples, the absorption bands of C = O and C = N peaks at 1736 and 1667 cm^{-1} and aliphatic CH

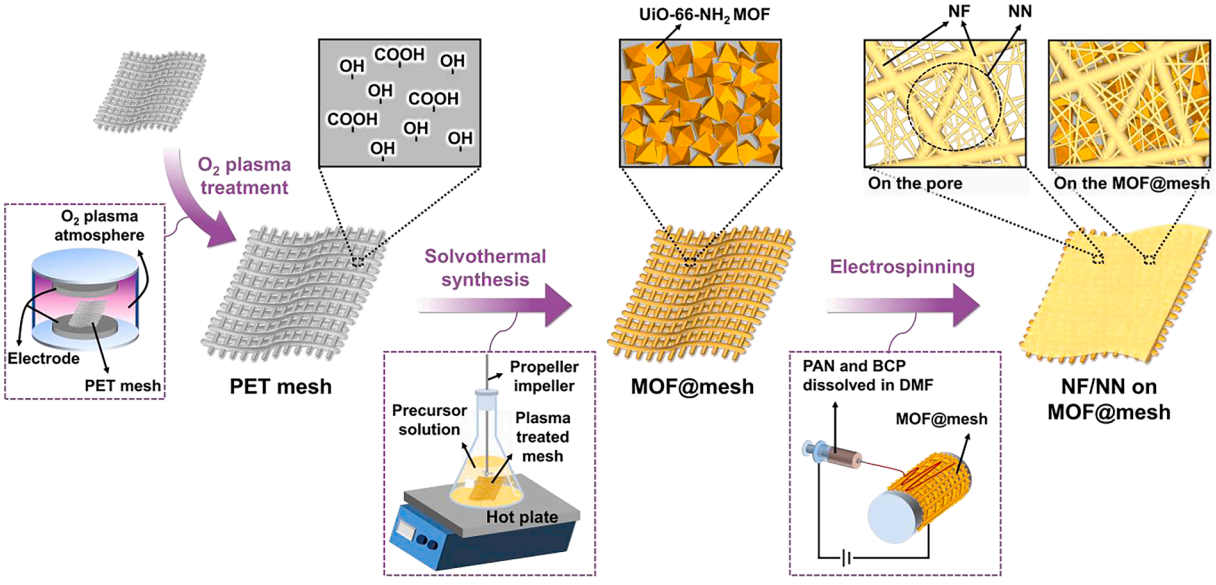

Fig. 1. Schematic of the fabrication procedure for the NF/NN on MOF@mesh filter.

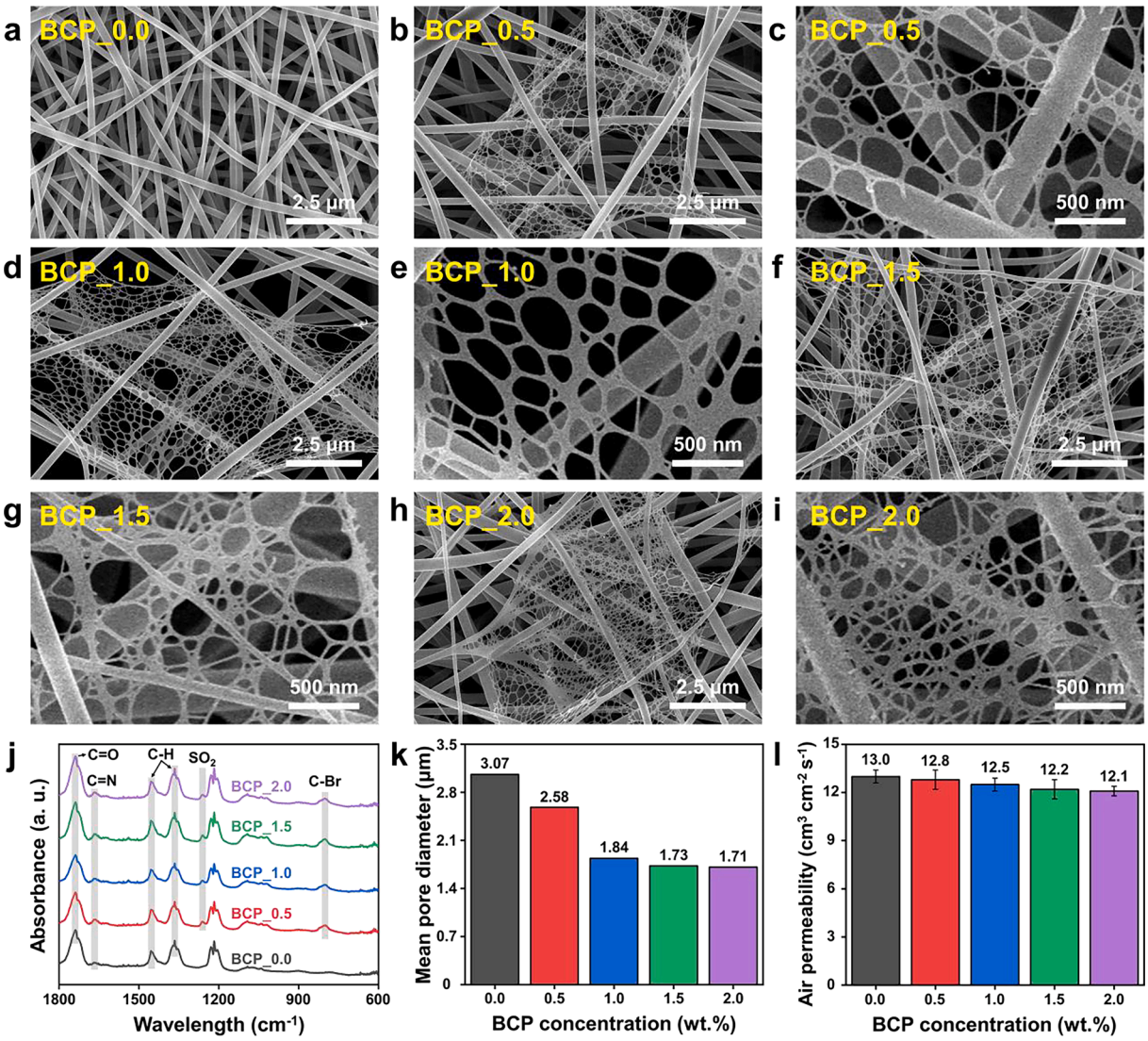

Fig. 2. Scanning electron microscopy (SEM) images of electrospun NF/NN membranes fabricated using BCP-added PAN solution with different BCP concentrations of (a) 0.0, (b, c) 0.5, (d, e) 1.0, (f, g) 1.5, and (h, i) 2.0 wt% at different magnifications. (j) Fourier transform infrared (FT-IR) absorption spectra, (k) mean pore diameters, and (l) air permeability of NF/NN membranes with different BCP concentrations.

peaks at 1454 and 1364 cm^{-1} are observed, corresponding to the PAN backbone.[30] The presence of SO_2 and C-Br peaks at 1259 and 800 cm^{-1} is attributed to the BCP component in the BCP-added samples.[31] The mean pore diameters of the samples (BCP_0.0, 0.5, 1.0, 1.5, and 2.0) were analyzed using capillary flow porosimetry. As shown in Fig. 2k, BCP-added membranes show sequentially reducing mean pore diameters of 2.58, 1.84, 1.73, and 1.71 μm for BCP_0.5, 1.0, 1.5, and 2.0, respectively, compared to the pristine PAN NF (30.7 μm). This trend is closely related to the formation of NN networks induced by BCP addition, as observed in the SEM images (Fig. 2a–2i).

Air permeability is a critical factor for determining the performance of air filters and is significantly affected by the microstructural evolution and thickness of fibrous membranes.[32] Air permeability significantly reduces with increasing electrospinning time (Fig. S4). For example, the air permeability is slightly reduced when BCP is added with an electrospinning time of 60 min (Fig. 2l), with negligible differences before and after BCP addition (less than 1 $cm^3\ cm^{-2}\ s^{-1}$). Although the partial formation of NNs reduces the average pore diameter, a relatively similar air permeability is obtained because of the three-dimensional pores in the membrane. Considering that a high air permeability is closely related to the small pressure drop of filters, the formation of NNs is expected to be beneficial for improving the overall filtration efficiency by capturing small dust particles while maintaining a low pressure drop.[33–35].

Various NF/NN-based membranes with different BCP concentrations and electrospinning durations (from 10 to 60 min) were prepared to evaluate the air filtration performance. As shown in Fig. 3a, each membrane exhibits distinct colors, depending on the controlled parameters. As the electrospinning time increases, the number of accumulated nanofibrous layers increases, leading to a decrease in the transparency of the membranes. Meanwhile, a distinct color change from white to deep yellow is observed with an increase in the BCP content. Accordingly, the relative transmittance declines proportionally with increasing BCP concentration in the visible wavelength range (Fig. S5).

The filtration efficiencies and pressure drops of the NF/NN membranes were assessed using the standard TSI 8130 equipment (Fig. S6). Filtration efficiency is expressed as the rate of aerosol particles of a certain size that can be clogged using a filtration system, and the pressure drop is the total pressure drop between two points in the fluid transport network. The filtration efficiency of all samples shows an almost linear increasing trend as the electrospinning time increases from 10 (28.1, 28.5, 31.1, 31.9, and 32.2% for BCP_0.0, 0.5, 1.0, 1.5, and 2.0, respectively) to 60 min (85.5, 90.6, 91.4, 93.1, and 93.6% for BCP_0.0,

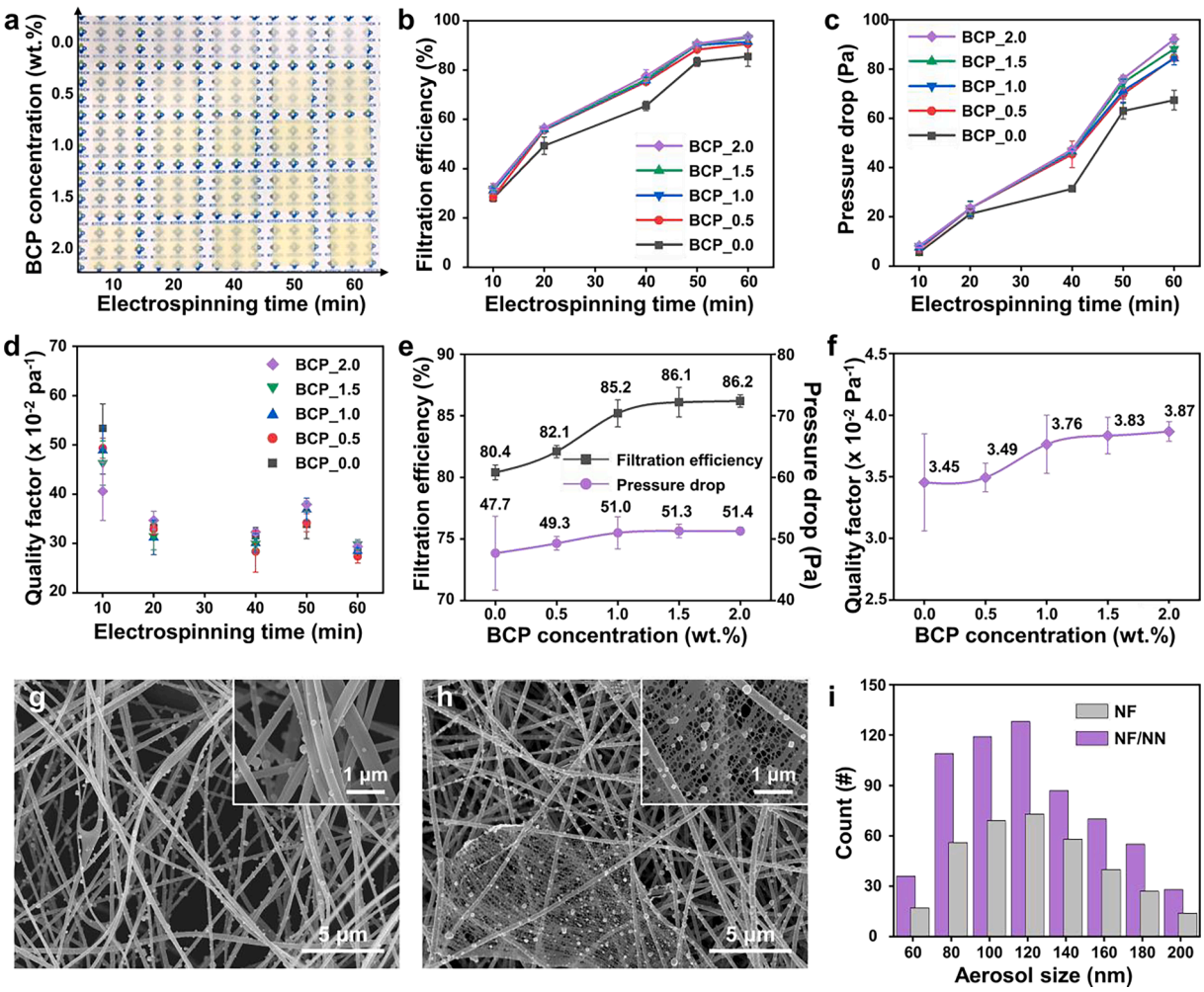

Fig. 3. (a) Photographs of various NF/NN on MOF@mesh filters with different electrospinning times and added BCP concentrations. (b) Filtration efficiency, (c) pressure drop, and (d) corresponding Q_f values of NF/NN on MOF@mesh filters with different electrospinning durations. (e) Filtration efficiency, pressure drop, and (f) corresponding Q_f values of NF/NN on MOF@mesh with different BCP concentrations (electrospinning time of these samples was set to be 50 min). SEM images of pristine (g) NF and (h) NF/NN membranes after filtration tests. (i) Size distributions of collected NaCl aerosol particles on NF and NF/NN membranes.

0.5, 1.0, 1.5, and 2.0, respectively) (Fig. 3b). Additionally, the pressure drop gradually decreases with increasing electrospinning time from 10 (5.6, 6.9, 7.5, 8.2, and 8.2 Pa for BCP_0.0, 0.5, 1.0, 1.5, and 2.0, respectively) to 60 min (47.7, 49.3, 51.0, 51.3, and 51.4 Pa for BCP_0.0, 0.5, 1.0, 1.5, and 2.0, respectively) (Fig. 3c).

Considering the filtration performance, the filtration efficiency generally exhibits a trade-off relationship with the pressure drop based on the physical sieving mechanism of fibrous membranes.[21] To achieve an optimal filtration performance, finding optimal values for the filtration efficiency and pressure drop is important. Generally, the quality of a filter is quantitatively determined using the Q_f, which can be calculated using the following equation:

$$Q_f = -\ln(1-\eta)/\Delta P \quad (3)$$

where η is the removal efficiency, and ΔP is the pressure drop.[34,36] The Q_f values of the prepared membranes are summarized in Table S1. The average Q_f values of the NF/NN membranes obtained after 50 min of electrospinning are relatively higher than those obtained under other conditions. Although the NF/NN membranes obtained after 10 min of electrospinning exhibit the highest average Q_f values, their filtration efficiencies are very low (~30%) and are not adequate for achieving effective PM removal.

Fig. 3e presents the filtration efficiency and pressure drop characteristics of the 50 min-electrospun NF/NN membranes with different BCP contents. The filtration efficiencies of the BCP-added samples are 82.1%, 85.2%, 86.1%, and 86.2% for BCP_0.5, 1.0, 1.5, and 2.0, respectively, which is evidently higher than that of pristine NF (BCP_0.0: 80.4%). Similarly, BCP-added samples demonstrate higher pressure drops in comparison with pristine NF (47.7 Pa) although the pressure drop is saturated to ~ 51.4 Pa after a 1.0% addition of BCP. This can be ascribed to the distribution of local NNs throughout the membrane regardless of BCP addition. In this regard, the Q_f values of the NF/NN membranes exhibit a gradual increase,[37] and the 2.0 wt% BCP-added NF/NN membrane yields the highest Q_f value of 0.0387 Pa^{-1} (Fig. 3f). To evaluate the stability and reusability of the membrane after the filtration performance test, we repeated three cycles of PM loading, washing with DI water for 1 min, and drying. When the BCP concentration further increased to 5 wt%, formation of NN was reduced, and the filtration efficiency and pressure decreased to 81.1% and 49.7 Pa, respectively (Fig. S7). Therefore, we selected BCP_2.0 as an optimized sample for further experiments. As depicted in Fig. S8a, the pressure gradually increased during PM loading for each cycle. Interestingly, the pressure at the ends of the first and second tests (55.9 and 51.9 Pa, respectively) were reduced further to 49.0 and 46.1 Pa after the first and second washing/drying steps. Furthermore, the initial filtration efficiency (86.2%) was considerably maintained at 85.4 and 81.9% after the first and second washing/drying steps, respectively. The SEM images of the membrane after cycle tests also confirmed that the unique NF/NN

structure of the pristine membrane was well preserved after PM loading and washing cycles (Fig. S8b and S8c). The slight reduction of filtration performance was mainly attributed to physical damage of the membrane sample during the sample loading and washing steps.

We further characterized the microstructure via the *ex-situ* observation of the membranes after the filtration tests. Fig. 3g and 3 h show the NaCl aerosol particles captured on the pristine NF (BCP_0.0) and NF/NN (BCP_2.0) membranes. Notably, a large number of aerosol particles are captured by the NN regions. Considering the physical sieving mechanism of fibrous filter media, the narrow voids between the in-plane fibers are more effective for capturing smaller particles. The size distribution and number of captured particles are summarized in Fig. 3i. The average diameters of captured particles are 121.3 and 123.4 nm for NN and NF/NN, respectively, and a significant increase in the number of particles with diameters less than 120 nm is observed for NF/NN. Furthermore, the overall number of particles collected in the NF/NN membrane is approximately 1.8-fold higher than that in the NN membrane. These results demonstrate that the as-formed NN exhibits high potential for removing ultrafine contaminants with sizes less than 100 nm ($PM_{0.1}$).

MOFs possess very large specific surface areas and tunable adsorption properties, which render them suitable for air purification applications via the selective adsorption of toxic gases. Zr-based UiO-66-NH_2 exhibits high adsorption capacity toward aldehyde gases, such as acetaldehyde, formaldehyde, propionaldehyde, and butyraldehyde, in addition to high thermal/chemical stability.[38] The gas adsorption capability is attributed to the formation of strong covalent bonds between the amine functional groups (–NH_2) in the organic linker of the MOFs and the carbonyl group of the aldehyde molecules.[39–41] Physicochemical properties were investigated for powder-type UiO-66-NH_2 MOF *via* SEM, XRD, and N_2 adsorption/desorption analyses for integrating it with the PET mesh substrate under optimized synthesis conditions. The fabricated UiO-66-NH_2 has an octahedral structure with a relatively uniform size of ~130 nm, which is similar to that reported previously in the literature (Fig. 4a).[42] The high degree of UiO-66-NH_2 dispersion is also beneficial for capturing gas phases.[43] In the XRD pattern of UiO-66-NH_2, the intense crystalline peaks at 7.3°, 8.5°, 17.0°, 25.6°, and 30.6° match well with the (111), (200), (400), (600), and (711) planes of UiO-66-NH_2, respectively (Fig. 4b).[42,44] The isotherm of UiO-66-NH_2 exhibits a type I shape (less than 2 nm in pore size) in the low-relative-pressure regions ($P P_0^{-1} \leq 0.85$), whereas certain type IV characteristics (2–50 nm pore size) are also observed in the high-relative-pressure regions ($P P_0^{-1} > 0.9$) (Fig. 4c).[45] This curve indicates a mixed-type I/IV isotherm, suggesting the coexistence of both micro- and mesoporous structures in the ordered organic and inorganic frameworks. Moreover, the Brunauer–Emmett–Teller (BET) surface area of the UiO-66-NH_2 powder is calculated to be 1310.3 $m^2 g^{-1}$, which is significantly higher than that of well-known porous adsorbents, such as activated carbon or zeolites (less than 1000 $m^2 g^{-1}$).[46,47] The large surface area provides numerous accessible sites for accommodating gaseous species, and the functionalization of MOFs with NH_2 can typically enhance the selective adsorption property toward CH_3CHO gas.

The low-magnification SEM image shows that the MOF@mesh had a similar morphology to the pristine mesh, with a slight color change to bright yellow (Fig. 4e and S1c). The surface of the MOF@mesh is uniformly covered by MOF particles (inset of Fig. 4d), while their original octahedral shape and size are maintained, as shown in Fig. 4a. This indicates that the direct growth method on the mesh does not affect the formation of nanocrystals. Additionally, relatively dense MOF crystals are distributed on the mesh, suggesting that the MOF particles strongly adhere to the O_2-treated PET mesh substrate.

To further demonstrate the effectiveness of the MOF@mesh structure, we prepared five different types of filter membranes; i) pristine mesh (mesh), ii) MOF-decorated mesh (MOF@mesh), iii) electrospun NF on the pristine mesh (NF on mesh), iv) electrospun NF on the MOF@mesh (NF on MOF@mesh), and iv) electro-sprayed MOFs on NF layers with a pristine mesh support (NF@MOF on mesh). The NF@MOF on mesh was prepared by electrospraying MOFs during the electrospinning of NF layers as described in a previous publication,[21] and its microstructure is shown in Fig. S9. The MOF@mesh shows a sufficiently high

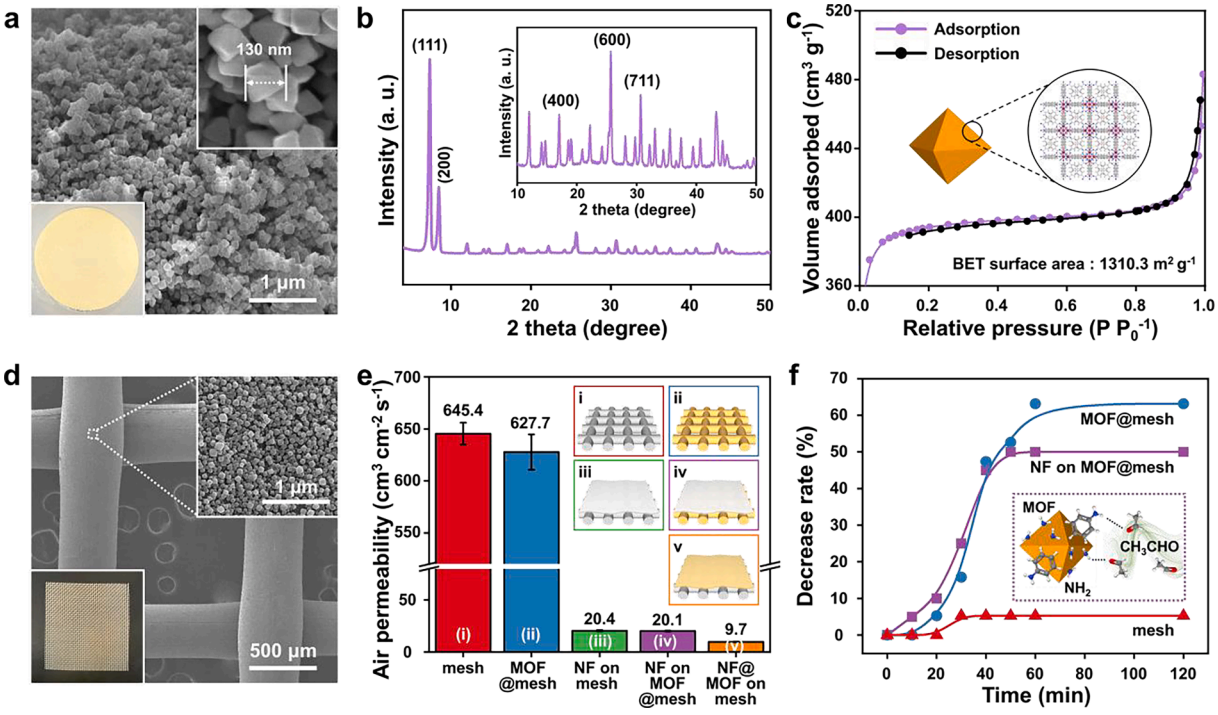

Fig. 4. (a) SEM and photographic images, (b) X-ray diffraction (XRD) patterns, and (c) N_2 adsorption–desorption isotherms for UiO-66-NH_2 MOFs. (d) SEM and photographic images of MOF@mesh. (e) Air permeability of various filters: i) pristine mesh, ii) MOF@mesh, iii) NF on mesh, iiv) NF on MOF@mesh, and iv) NF@MOF on mesh. (f) CH_3CHO concentration decrease rate for pristine mesh, MOF@mesh, and NF on MOF@mesh.

air permeability of 627.7 cm^3 cm^{-2} s^{-1} compared to that of the pristine mesh (645.4 cm^3 cm^{-2} s^{-1}) (Fig. 4f). Conversely, the introduction of the NF layer significantly reduces the air permeability, with NF on mesh and NF on MOF@mesh exhibiting air permeability values of 20.4 and 20.1 cm^3 cm^{-2} s^{-1}, respectively. Notably, the air permeability of NF@MOF on mesh (9.7 cm^3 cm^{-2} s^{-1}) is approximately 2-fold lower than that of NF on MOF@mesh (20.1 cm^3 cm^{-2} s^{-1}). This implies that the introduction of additives in the NF layers significantly reduces the air permeability because of the pore-clogging of the fine pores between the NFs. Therefore, the design of stacked filter layers is crucial for achieving appropriate filtration performance when functional materials are introduced and our novel method for the direct MOF growth on a wide supporting mesh can be an ideal approach for constructing a multifunctional filter platform.

To evaluate the gas adsorption properties of UiO-66-NH_2 on the mesh, we monitored the concentration of CH_3CHO in a Tedlar® gas bag with a gas detector (Fig. S10) before and after inserting various samples (pristine mesh, MOF@mesh, and NF on MOF@mesh). The concentration decrease rate (CDR) of the exposed gas (CH_3CHO) with respect to the elapsed time was monitored for the pristine mesh, MOF@mesh, and NF on MOF@mesh (Fig. 4f). The pristine mesh exhibits only a 5.3% reduction in the CH_3CHO content, whereas MOF@mesh shows high CDRs, achieving a 63.2% reduction within 60 min. This indicates that the UiO-66-NH_2 MOF has strong interactions with CH_3CHO, including both physisorption, via van der Waals force,[22,39,48] and chemisorption, via hydrogen bonding between the oxygen species in CH_3CHO and amine group (NH_2).[49,50] The NF on MOF@mesh shows high CDRs at the beginning, and the curve saturates at 52.9% after 50 min, indicating the strong interactions between CH_3CHO and MOF, although the adsorption sites of MOF@mesh are partially covered by the NF layers. These results demonstrate that the MOF@mesh serves as a robust NF support layer with sufficient air permeability and provides additional CH_3CHO gas removal capability. We further verified whether other control factors or functions (e.g., moisture, captured PM aerosol, and NH_3 gas detection) interfered with the filter original adsorption property. As shown in Fig. S11a, the CDR was 70.6% at 20% relative humidity (20% RH) and 26% and 31.6% after 60 and 120 min, respectively, at 50% RH. In addition, there was a slight decrease in CDR from 50.0% to 44.4% at 120 min after PM loading (Fig. S11b). As shown in Fig. S11c, slightly lower CDR values (less than 5%) were observed at the early stage of adsorption, but the normal level CDR was achieved at the final stage. In conclusion, it was experimentally demonstrated that the developed NF/NN on MOF@mesh exhibits independent performance for PM aerosol capture, NH_3 gas detection, and CH_3CHO adsorption without interference between the functions, although CH_3CHO adsorption performance was degraded by high humidity. [51,52] To investigate the regenerative feature of CH_3CHO adsorption, we dried the sample at 50 °C (similar to the temperature of a hair dryer) and repeated the adsorption tests. After three cycles of treatment and testing, the adsorption properties of MOF@mesh were regenerated (Fig. S12).

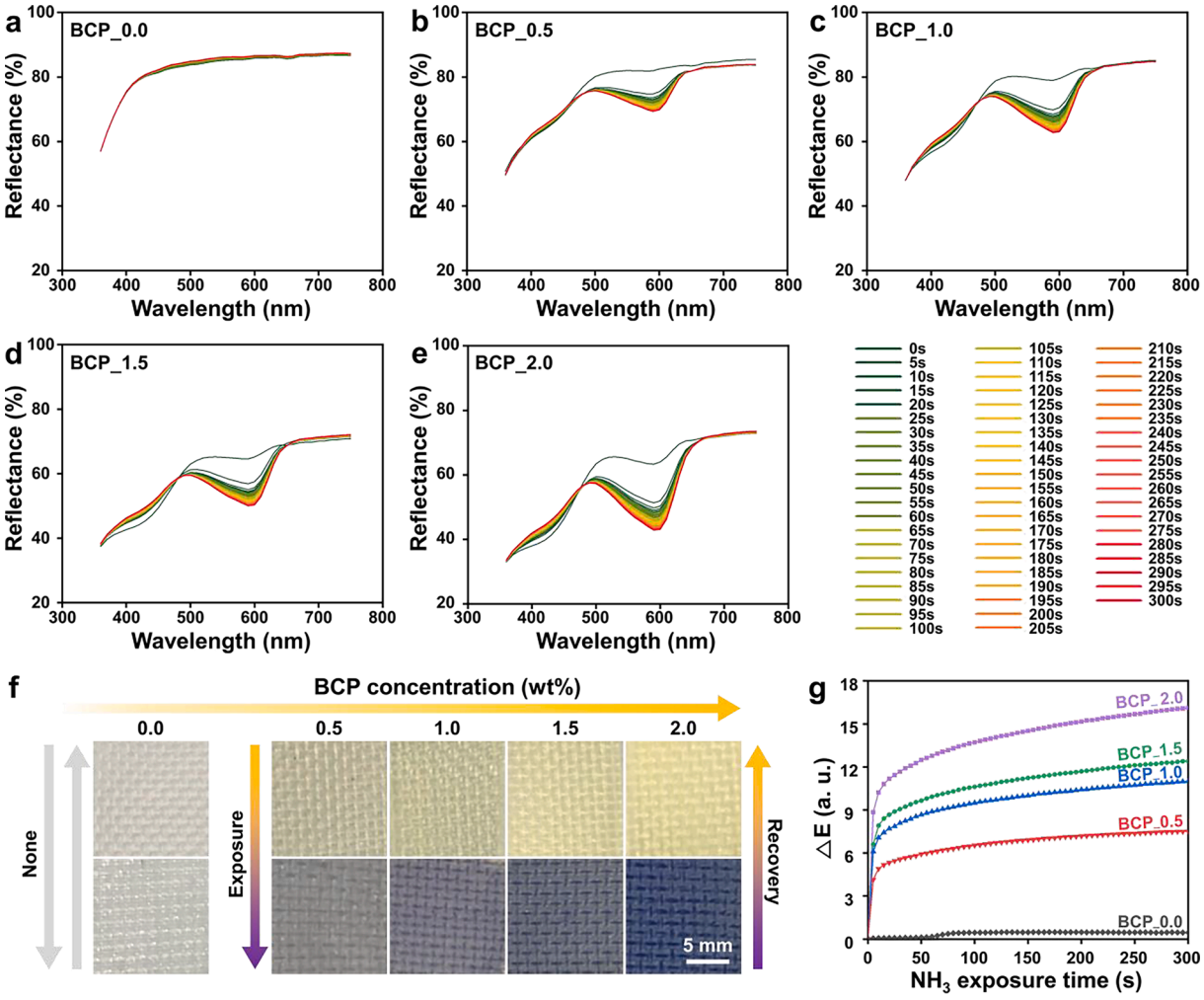

Fig. 5. Time-dependent reflectance of NF/NN on MOF@mesh filters with different BCP concentrations of (a) 0.0, (b) 0.5, (c) 1.0, (d) 1.5, and (e) 2.0 wt% with the exposure to 20 ppm NH_3 gas. (f) Photographic images of color changes for each filter after exposure to NH_3 gas, and (g) ΔE of NF/NN on MOF@mesh filters depending on various BCP concentrations and NH_3 gas exposure durations.

NH_3 gas-sensing tests were performed with NF/NN on MOF@mesh filters with various BCP contents. Fig. 5a–e present the time-dependent reflectance of the five filters containing various BCP concentrations (0.0, 0.5, 1.0, 1.5, and 2.0 wt%). Individual reflectance data were collected at 5 s-intervals for 300 s under exposure to 20 ppm NH_3 gas. The reflectance of all samples, except BCP_0.0, decreases sharply at approximately 600 nm and apparently decrease as the exposure time and BCP content increase. The reflectance changes can be explained by the deprotonation of BCP by amines, with protons migrating from the hydroxyl group of the BCP molecule to the nitrogen on the amine molecule. This reversible color change is consistent with the halochromic properties upon a change in the external stimulus.[53].

To confirm the immediate and reversible color change, photographic images of the filters were captured before and after exposure to NH_3 gas of 20 ppm (Fig. 5f). The color change from light yellow to purple or from purple to light yellow is observed within 5 s upon the exposure or removal of NH_3 (Supporting Video 1). The color change is more evident in samples with a higher BCP content, whereas no response is observed for BCP_0.0 toward NH_3 exposure and removal. The time dependence of the quantitative color differences (ΔE) was compared for filters with different BCP concentrations (Fig. 5g); details of the quantitative assessment are included in the experimental section. In general, $\Delta E > 3.3$ is the standard for determining whether the difference between two colors can be visually perceived by the naked eye.[54] The BCP_0.0 filter showed negligible ΔE change, while the BCP-added specimens showed a rapid increase in ΔE, exceeding 3.3 within 5 s, with values of 4.14, 6.11, 6.59, and 8.84 for BCP_0.5, 1.0, 1.5, and 2.0, respectively. As shown in Fig. S13, these behaviors were observed even in the presence of aerosols on NF/NN membranes. Moreover, the overall time-dependent ΔE increased with increasing BCP content, mainly due to the increase in reactive components and active surface area. However, ΔE decreases with continuous exposure to gas compared to the initial increasing trend, which is ascribed to the reversible reaction of NH_3 and BCP or the rapid diffusion and transport of the low-concentration gas into the atmosphere.[55–57] The results confirm that the as-fabricated NF/NN on MOF@mesh filter can immediately react with harmful NH_3 gas even at 20 ppm with high reversibility.[58] In addition, we carried out additional colorimetric sensing tests at an extremely low concentration of NH_3 gas (1 ppm) to evaluate the detection limit of our sample. As shown in Fig. S14a, there were obvious changes in reflectance of BCP_2.0 after exposure to 1 ppm NH_3. The ΔE of BCP_2.0 as a function of NH_3 exposure time exceeds 3.31 at around 60 s even at 1 ppm NH_3 (Fig. S14b). This means that the difference between two colors induced by exposure to 1 ppm of NH_3 can be visually perceived within 1 min by the naked eye.

The NF/NN on MOF@mesh filter has a high potential for application as a window filter for simultaneously removing particulates and detecting gaseous contaminants. Fig. 6a shows the real samples attached to a glass window, and the outdoor landscape can be observed through the filters. A schematic illustrating the functions of the NF/NN on MOF@mesh filter when applied as a window filter to maintain indoor air quality is presented in Fig. 6b. The incoming PMs ($PM_{2.5}$ and even $PM_{1.0}$) and fine dust particles can be effectively sieved using the NF/NN membrane. Additionally, toxic gases, such as aldehydes, from both the outside and inside of the building can be filtered using finely coated adsorptive MOFs on the mesh. Furthermore, the filter can be used as a colorimetric sensor for the detection of small amounts of toxic gases. The detailed functions of the NF/NN on MOF@mesh filter are summarized in Fig. 6c. The NF/NN on MOF@mesh with hybrid nanomaterials, including NFs and MOFs, can be utilized in various indoor environments, such as households and office buildings, as well as in various industrial fields, where PM and VOC concentrations should be simultaneously controlled.

4. Conclusions

We successfully demonstrated a NF/NN on MOF@mesh filter as a novel hybrid air filtration platform, which was achieved *via* a combination of BCP-added NF/NN and an adsorptive MOF-grown mesh substrate. By simply adding BCP to the electrospinning solution, a hybrid NN structure was spontaneously formed between the randomly entangled NFs, leading to a significant improvement in ultrafine dust filtration performance and filtration efficiency. The NF/NN membrane was supported on a UiO-66-NH_2 coated PET mesh, and the MOFs provide the additional function of CH_3CHO adsorption. Furthermore, the developed filter effectively detected a small amount of NH_3 (20 ppm) through a sensitive color change of the BCP components in NF/NN. This multifunctional filter can be applied as a window filter for maintaining a high-quality indoor atmosphere in households or offices. Furthermore, the novel strategy for combining adsorptive MOFs and electrospun NFs

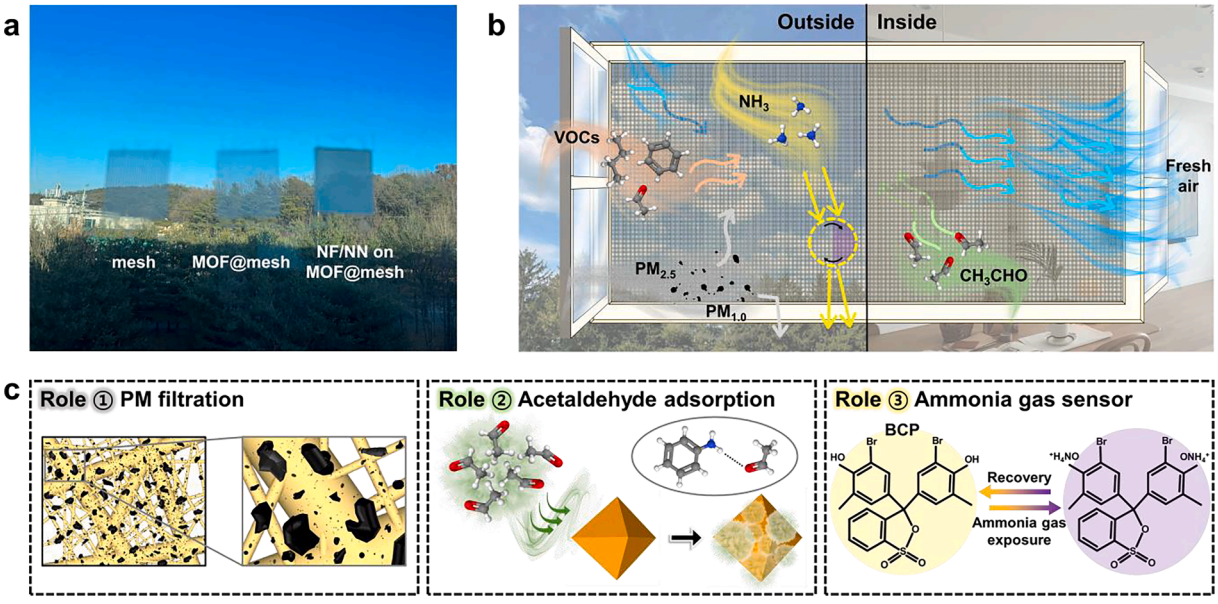

Fig. 6. (a) Photographic images of pristine mesh, MOF@mesh, and NF/NN on MOF@mesh filters attached on a glass window. (b) Schematic and (c) specific functions of NF/NN on MOF@mesh filters as a hybrid window filter.

suggested herein can be widely employed for various industrial air filtration applications requiring the simultaneous control of various PMs and toxic gases.

Declaration of Competing Interest

The authors declare that they have no known competing financial interests or personal relationships that could have appeared to influence the work reported in this paper.

Data availability

Data will be made available on request.

Acknowledgements

This study has been conducted with the supports of the Korea Institute of Industrial Technology as "Development of fiber-based technology for reduction of hazardous substances in the air (kitech EO-22-0002)". This work was also supported by the Technology development Program (S2798904) funded by the Ministry of SMEs and Startups (MSS, Korea). This work was also supported by National Research Foundation of Korea (NRF) grant funded by the Korean government (MSIT) (No. 2022M3C1C3095083).

Appendix A. Supplementary data

Supplementary data to this article can be found online at https://doi.org/10.1016/j.cej.2023.142725.

References

[1] M.C. Turner, Z.J. Andersen, A. Baccarelli, W.R. Diver, S.M. Gapstur, C.A. Pope III, D. Prada, J. Samet, G. Thurston, A. Cohen, Outdoor air pollution and cancer: an overview of the current evidence and public health recommendations, CA Cancer J. Clin. 70 (6) (2020) 460–479, https://doi.org/10.3322/caac.21632.

[2] G. Zhu, X. Wang, T. Yang, J. Su, Y. Qin, S. Wang, M. Gillings, C. Wang, F. Ju, B. Lan, Air pollution could drive global dissemination of antibiotic resistance genes, ISME J. 15 (1) (2021) 270–281, https://doi.org/10.1038/s41396-020-00780-2.

[3] B.C. McDonald, J.A.d. Gouw, J.B. Gilman, S.H. Jathar, A. Akherati, C.D. Cappa, J.L. Jimenez, J. Lee-Taylor, P.L. Hayes, S.A. McKeen, Y.Y. Cui, S.-W. Kim, D.R. Gentner, G. Isaacman-VanWertz, A.H. Goldstein, R.A. Harley, G.J. Frost, J.M. Roberts, T.B. Ryerson, M. Trainer, Volatile chemical products emerging as largest petrochemical source of urban organic emissions, Science 359(6377) (2018) 760-764, 10.1126/science.aaq0524.

[4] R. Dryden, M.G. Morgan, A. Bostrom, W. Bruine de Bruin, Public perceptions of how long air pollution and carbon dioxide remain in the atmosphere, Risk Anal. 38 (3) (2018) 525–534, https://doi.org/10.1111/risa.12856.

[5] T. Huang, X. Zhu, Q. Zhong, X. Yun, W. Meng, B. Li, J. Ma, E.Y. Zeng, S. Tao, Spatial and Temporal Trends in Global Emissions of Nitrogen Oxides from 1960 to 2014, Environ. Sci. Technol. 51 (14) (2017) 7992–8000, https://doi.org/10.1021/acs.est.7b02235.

[6] Q. Zhong, H. Shen, X. Yun, Y. Chen, Y.a. Ren, H. Xu, G. Shen, W. Du, J. Meng, W. Li, J. Ma, S. Tao, Global Sulfur Dioxide Emissions and the Driving Forces, Environ. Sci. Technol. 54(11) (2020) 6508-6517, 10.1021/acs.est.9b07696.

[7] I. Abbas, G. Badran, A. Verdin, F. Ledoux, M. Roumié, D. Courcot, G. Garçon, Polycyclic aromatic hydrocarbon derivatives in airborne particulate matter: sources, analysis and toxicity, Environ. Chem. Lett. 16 (2) (2018) 439–475, https://doi.org/10.1007/s10311-017-0697-0.

[8] G.-H. Zhang, Q.-H. Zhu, L. Zhang, F. Yong, Z. Zhang, S.-L. Wang, Y. Wang, L. He, G.-H. Tao, High-performance particulate matter including nanoscale particle removal by a self-powered air filter, Nat. Commun. 11 (1) (2020) 1–10, https://doi.org/10.1038/s41467-020-15502-7.

[9] Y. Zhang, Z. Zhu, W.-N. Wang, S.-C. Chen, Mitigating the relative humidity effects on the simultaneous removal of VOCs and PM2. 5 of a metal–organic framework coated electret filter, Sep. Purif. Technol. 285 (2022) 120309, 10.1016/j.seppur.2021.120309.

[10] E. Carter, C. Norris, K.L. Dionisio, K. Balakrishnan, W. Checkley, M.L. Clark, S. Ghosh, D.W. Jack, P.L. Kinney, J.D. Marshall, Assessing exposure to household air pollution: a systematic review and pooled analysis of carbon monoxide as a surrogate measure of particulate matter, Environ. Health Perspect. 125 (7) (2017), 076002, https://doi.org/10.1289/EHP767.

[11] Y. Bian, R. Wang, S. Wang, C. Yao, W. Ren, C. Chen, L. Zhang, Metal–organic framework-based nanofiber filters for effective indoor air quality control, J. Mater. Chem. A 6 (32) (2018) 15807–15814, https://doi.org/10.1039/C8TA04539A.

[12] F.H. Tang, M. Lenzen, A. McBratney, F. Maggi, Risk of pesticide pollution at the global scale, Nat. Geosci. 14 (4) (2021) 206–210, https://doi.org/10.1038/s41561-021-00712-5.

[13] V.V. Tran, D. Park, Y.-C. Lee, Indoor air pollution, related human diseases, and recent trends in the control and improvement of indoor air quality, Int. J. Environ. Res. Public Health 17 (8) (2020) 2927, https://doi.org/10.3390/ijerph17082927.

[14] Y. Dou, W. Zhang, A. Kaiser, Electrospinning of metal-organic frameworks for energy and environmental applications, Adv. Sci. 7 (3) (2020) 1902590, https://doi.org/10.1002/advs.201902590.

[15] N.P.B. Tan, S.S. Paclijan, H.N.M. Ali, C.M.J.S. Hallazgo, C.J.F. Lopez, Y.C. Ebora, Solution blow spinning (SBS) nanofibers for composite air filter masks, ACS Appl. Nano Mater. 2 (4) (2019) 2475–2483, https://doi.org/10.1021/acsanm.9b00207.

[16] S. Ullah, A. Ullah, J. Lee, Y. Jeong, M. Hashmi, C. Zhu, K.I. Joo, H.J. Cha, I.S. Kim, Reusability comparison of melt-blown vs nanofiber face mask filters for use in the coronavirus pandemic, ACS Appl. Nano Mater. 3 (7) (2020) 7231–7241, https://doi.org/10.1021/acsanm.0c01562.

[17] Y. Chen, S. Zhang, S. Cao, S. Li, F. Chen, S. Yuan, C. Xu, J. Zhou, X. Feng, X. Ma, B. Wang, Roll-to-roll production of metal-organic framework coatings for particulate matter removal, Adv. Mater. 29 (15) (2017), https://doi.org/10.1002/adma.201606221.

[18] D.K. Yoo, H.C. Woo, S.H. Jhung, Effective removal of particulate matter from air by using zeolite-coated filters, J. Mater. Chem. A 8 (35) (2020) 17960–17968, https://doi.org/10.1039/D0TA04914J.

[19] H.C. Woo, D.K. Yoo, S.H. Jhung, Highly improved performance of cotton air filters in particulate matter removal by the incorporation of metal-organic frameworks with functional groups capable of large charge separation, ACS Appl. Mater. Interfaces 12 (25) (2020) 28885–28893, https://doi.org/10.1021/acsami.0c07123.

[20] X. Wang, W. Xu, X. Yan, Y. Chen, M. Guo, G. Zhou, S. Tong, M. Ge, Y. Liu, C. Chen, MOF-based fibrous membranes adsorb PM efficiently and capture toxic gases selectively, Nanoscale 11 (38) (2019) 17782–17790, https://doi.org/10.1039/C9NR05795A.

[21] D. Kim, Y. Kim, D. Kim, D. Son, S.J. Doh, M. Kim, H. Lee, K.R. Yoon, Rational Process Design for Facile Fabrication of Dual Functional Hybrid Membrane of MOF and Electrospun Nanofiber towards High Removal Efficiency of $PM_{2.5}$ and Toxic Gases, Macromol. Rapid Commun. 43 (2021) 2100648, 10.1002/marc.202100648.

[22] Y. Zhang, S. Yuan, X. Feng, H. Li, J. Zhou, B. Wang, Preparation of nanofibrous metal-organic framework filters for efficient air pollution control, J. Am. Chem. Soc. 138 (18) (2016) 5785–5788, https://doi.org/10.1021/jacs.6b02553.

[23] F. Khelifa, S. Ershov, Y. Habibi, R. Snyders, P. Dubois, Free-radical-induced grafting from plasma polymer surfaces, Chem. Rev. 116 (6) (2016) 3975–4005, https://doi.org/10.1021/acs.chemrev.5b00634.

[24] G. Yang, X. Li, Y. He, J. Ma, G. Ni, S. Zhou, From nano to micro to macro: electrospun hierarchically structured polymeric fibers for biomedical applications, Prog. Polym. Sci. 81 (2018) 80–113, https://doi.org/10.1016/j.progpolymsci.2017.12.003.

[25] T. Xu, Y. Ding, Z. Liang, H. Sun, F. Zheng, Z. Zhu, Y. Zhao, H. Fong, Three-dimensional monolithic porous structures assembled from fragmented electrospun nanofiber mats/membranes: methods, properties, and applications, Prog. Mater. Sci. 112 (2020), 100656, https://doi.org/10.1016/j.pmatsci.2020.100656.

[26] A.M. Al-Dhahebi, S.C.B. Gopinath, M.S.M. Saheed, Graphene impregnated electrospun nanofiber sensing materials: a comprehensive overview on bridging laboratory set-up to industry, Nano Converg. 7 (1) (2020) 1–23, https://doi.org/10.1186/s40580-020-00237-4.

[27] J. Zhang, L. Liu, Y. Si, J. Yu, B. Ding, Electrospun nanofibrous membranes: an effective arsenal for the purification of emulsified oily wastewater, Adv. Funct. Mater. 30 (25) (2020) 2002192, https://doi.org/10.1002/adfm.202002192.

[28] H. Liu, S. Zhang, L. Liu, J. Yu, B. Ding, High-Performance PM0.3 Air Filters Using Self-Polarized Electret Nanofiber/Nets, Adv. Funct. Mater. 30(13) (2020) 1909554, 10.1002/adfm.201909554.

[29] S. Bhattacharya, I. Roy, A. Tice, C. Chapman, R. Udangawa, V. Chakrapani, J. L. Plawsky, R.J. Linhardt, High-conductivity and high-capacitance electrospun fibers for supercapacitor applications, ACS Appl. Mater. Interfaces 12 (17) (2020) 19369–19376, https://doi.org/10.1021/acsami.9b21696.

[30] J. Li, D. Zhang, T. Yang, S. Yang, X. Yang, H. Zhu, Nanofibrous membrane of graphene oxide-in-polyacrylonitrile composite with low filtration resistance for the effective capture of PM2.5, J. Membr. Sci. 551 (2018) 85–92, https://doi.org/10.1016/j.memsci.2018.01.025.

[31] I. Sousa, M.C. Quevedo, A. Sushkova, M.G.S. Ferreira, J. Tedim, Chitosan microspheres as carriers for pH-indicating species in corrosion sensing, Macromol. Mater. Eng. 305 (2) (2020) 1900662, https://doi.org/10.1002/mame.201900662.

[32] H. Liu, S. Zhang, L. Liu, J. Yu, B. Ding, A fluffy dual-network structured nanofiber/net filter enables high-efficiency air filtration, Adv. Funct. Mater. 29 (39) (2019) 1904108, https://doi.org/10.1002/adfm.201904108.

[33] D.-H. Kim, J. Bae, J. Lee, J. Ahn, W.-T. Hwang, J. Ko, I.-D. Kim, Porous nanofiber membrane: rational platform for highly sensitive thermochromic sensor, Adv. Funct. Mater. 32 (24) (2022) 2200463, https://doi.org/10.1002/adfm.202200463.

[34] W.T. Koo, Y. Hong, D. Joung, C. Kim, Surface hydration of fibrous filters by using water-absorbing metal–organic frameworks for efficient ultrafine particulate matter removal, Chem. Eng. J. 446 (2022), 136710, https://doi.org/10.1016/j.cej.2022.136710.

[35] S. Zhang, H. Liu, J. Yu, B. Li, B. Ding, Multi-functional flexible 2D carbon nanostructured networks, Nat. Commun. 11 (1) (2020) 1–8, https://doi.org/10.1038/s41467-020-18977-6.

[36] J. Lee, J. Bae, D.-Y. Youn, J. Ahn, W.-T. Hwang, H. Bae, P.K. Bae, I.-D. Kim, Violacein-embedded nanofiber filters with antiviral and antibacterial activities, Chem. Eng. J. 444 (2022), 136460, https://doi.org/10.1016/j.cej.2022.136460.
[37] B. Cheng, Z. Li, Q. Li, J. Ju, W. Kang, M. Naebe, Development of smart poly (vinylidene fluoride)-graft-poly (acrylic acid) tree-like nanofiber membrane for pH-responsive oil/water separation, J. Membr. Sci. 534 (2017) 1–8, https://doi.org/10.1016/j.memsci.2017.03.053.
[38] K. Vikrant, Y. Qu, J.E. Szulejko, V. Kumar, K. Vellingiri, D.W. Boukhvalov, T. Kim, K.-H. Kim, Utilization of metal–organic frameworks for the adsorptive removal of an aliphatic aldehyde mixture in the gas phase, Nanoscale 12 (15) (2020) 8330–8343, https://doi.org/10.1039/D0NR00234H.
[39] K. Vellingiri, P. Kumar, A. Deep, K.-H. Kim, Metal-organic frameworks for the adsorption of gaseous toluene under ambient temperature and pressure, Chem. Eng. J. 307 (2017) 1116–1126, https://doi.org/10.1016/j.cej.2016.09.012.
[40] K. Vikrant, M. Cho, A. Khan, K.-H. Kim, W.-S. Ahn, E.E. Kwon, Adsorption properties of advanced functional materials against gaseous formaldehyde, Environ. Res. 178 (2019), 108672, https://doi.org/10.1016/j.envres.2019.108672.
[41] A. Khan, J.E. Szulejko, K.-H. Kim, P. Sammadar, S.S. Lee, X. Yang, Y.S. Ok, A comparison of figure of merit (FOM) for various materials in adsorptive removal of benzene under ambient temperature and pressure, Environmental Research 168 (2019) 96–108, https://doi.org/10.1016/j.envres.2018.09.019.
[42] J. Zhang, Y. Hu, J. Qin, Z. Yang, M. Fu, TiO2-UiO-66-NH2 nanocomposites as efficient photocatalysts for the oxidation of VOCs, Chem. Eng. J. 385 (2020), 123814, https://doi.org/10.1016/j.cej.2019.123814.
[43] H. Wang, S. Zhao, Y. Liu, R. Yao, X. Wang, Y. Cao, D. Ma, M. Zou, A. Cao, X. Feng, B. Wang, Membrane adsorbers with ultrahigh metal-organic framework loading for high flux separations, Nat. Commun. 10 (1) (2019) 4204, https://doi.org/10.1038/s41467-019-12114-8.
[44] D. Azarifar, R. Ghorbani-Vaghei, S. Daliran, A.R. Oveisi, A multifunctional zirconium-based metal-organic framework for the one-pot tandem photooxidative passerini three-component reaction of alcohols, ChemCatChem 9 (11) (2017) 1992–2000, https://doi.org/10.1002/cctc.201700169.
[45] H. Xue, X. Wang, Q. Xu, F. Dhaouadi, L. Sellaoui, M.K. Seliem, A. Ben Lamine, H. Belmabrouk, A. Bajahzar, A. Bonilla-Petriciolet, Z. Li, Q. Li, Adsorption of methylene blue from aqueous solution on activated carbons and composite prepared from an agricultural waste biomass: A comparative study by experimental and advanced modeling analysis, Chem. Eng. J. 430 (2022) 132801, 10.1016/j.cej.2021.132801.
[46] S. Lu, R. Han, H. Wang, C. Song, N. Ji, X. Lu, D. Ma, Q. Liu, Three birds with one stone: designing a novel binder-free monolithic zeolite pellet for wet VOC gas adsorption, Chem. Eng. J. 448 (2022), 137629, https://doi.org/10.1016/j.cej.2022.137629.
[47] A. Jain, M. Ghosh, M. Krajewski, S. Kurungot, M. Michalska, Biomass-derived activated carbon material from native European deciduous trees as an inexpensive and sustainable energy material for supercapacitor application, J. Energy Storage 34 (2021), 102178, https://doi.org/10.1016/j.est.2020.102178.
[48] Y. Zhang, X. He, Z. Zhu, W.-N. Wang, S.-C. Chen, Simultaneous removal of VOCs and PM2. 5 by metal-organic framework coated electret filter media, J. Membr. Sci. 618 (2021) 118629, 10.1016/j.memsci.2020.118629.
[49] K. Vikrant, Y.-X. Deng, K.-H. Kim, S.A. Younis, D.W. Boukhvalov, W.-S. Ahn, A. Deep, Application of Zr-cluster-based MOFs for the adsorptive removal of aliphatic aldehydes (C1 to C5) from an industrial solvent, ACS Appl. Mater. Interfaces 11 (47) (2019) 44270–44281, https://doi.org/10.1021/acsami.9b15220.
[50] I. Ahmed, S.H. Jhung, Effective adsorptive removal of indole from model fuel using a metal-organic framework functionalized with amino groups, J. Hazard. Mater. 283 (2015) 544–550, https://doi.org/10.1016/j.jhazmat.2014.10.002.
[51] J. Lee, D. Ka, H. Jung, K. Cho, Y. Jin, M. Kim, UiO-66-NH2 and zeolite-templated carbon composites for the degradation and adsorption of nerve agents, Molecules 26 (13) (2021) 3837, https://doi.org/10.3390/molecules26133837.
[52] X. Shi, X. Zhang, F. Bi, Z. Zheng, L. Sheng, J. Xu, Z. Wang, Y. Yang, Effective toluene adsorption over defective UiO-66-NH2: An experimental and computational exploration, J. Mol. Liq. 316 (2020), 113812, https://doi.org/10.1016/j.molliq.2020.113812.
[53] M.I. Khazi, W. Jeong, J.M. Kim, Functional materials and systems for rewritable paper, Adv. Mater. 30 (15) (2018) 1705310, https://doi.org/10.1002/adma.201705310.
[54] D.-H. Kim, J.-H. Cha, J.Y. Lim, J. Bae, W. Lee, K.R. Yoon, C. Kim, J.-S. Jang, W. Hwang, I.-D. Kim, Colorimetric dye-loaded nanofiber yarn: eye-readable and weavable gas sensing platform, ACS Nano 14 (12) (2020) 16907–16918, https://doi.org/10.1021/acsnano.0c05916.
[55] Y.K. Park, H.J. Oh, H.D. Lee, J.J. Lee, J.H. Kim, W. Lee, Facile and eco-friendly fabrication of a colorimetric textile sensor by UV-induced photografting for acidic gas detection, J. Environ. Chem. Eng. 10 (5) (2022), 108508, https://doi.org/10.1016/j.jece.2022.108508.
[56] E. Schoolaert, R. Hoogenboom, K. De Clerck, Colorimetric nanofibers as optical sensors, Adv. Funct. Mater. 27 (38) (2017) 1702646, https://doi.org/10.1002/adfm.201702646.
[57] J. Geltmeyer, G. Vancoillie, I. Steyaert, B. Breyne, G. Cousins, K. Lava, R. Hoogenboom, K. De Buysser, K. De Clerck, Dye modification of nanofibrous silicon oxide membranes for colorimetric HCl and NH3 sensing, Adv. Funct. Mater. 26 (33) (2016) 5987–5996, https://doi.org/10.1002/adfm.201602351.
[58] H.J. Oh, B.J. Yeang, Y.K. Park, H.J. Choi, J.H. Kim, Y.S. Kang, Y. Bae, J.Y. Kim, S. J. Lim, W. Lee, W.G. Hahm, Washable colorimetric nanofiber nonwoven for ammonia gas detection, Polymers 12 (7) (2020), https://doi.org/10.3390/polym12071585.